Supplementary Methods

In Vivo Electrophysiology Recording Paradigms

Neural activity from the ADn was recorded in freely moving mice across three distinct behavioral paradigms designed to probe different aspects of histaminergic modulation.

Paradigm 1: Pharmacological Manipulation in an Open Field. This paradigm assessed the tonic effect of systemic histaminergic manipulation on baseline HD cell activity. Mice were intraperitoneally (i.p.) injected with saline and then connected to the recording headstage. After a 10-minute recovery period in their home cage, neural activity was recorded for 10 minutes while the mouse explored a familiar, empty open field. The mouse was then returned to its home cage for a 60-minute rest period. Following this, it received an i.p. injection of DCZ (100 μg/kg), was reconnected to the headstage, and after a 10-minute recovery, a second 10-minute recording session was conducted in the same open field.

Paradigm 2: Naturalistic Object Exploration and Displacement. This paradigm assessed the dynamic response of HD cells to the introduction and spatial displacement of a novel object without pharmacological intervention. Mice were connected to the recording headstage and neural activity was first recorded for 10 minutes in an empty open field (Baseline session). The mouse was then briefly removed and placed in a resting cage for 5 minutes, during which a single novel object was introduced into the arena. The mouse was returned to the now object-containing arena for a 15-minute recording session (Object Novelty session). After another 5-minute rest period for the mouse, the object was moved to a novel location within the arena. The mouse was returned for a final 15-minute recording session (Object Displacement session).

Paradigm 3: Pharmacological Manipulation during Object Exploration. This paradigm assessed the effect of histaminergic manipulation specifically during object-based spatial processing. The protocol was identical to Paradigm 1, with the key difference that both recording sessions (post-saline and post-DCZ injection) were conducted in an open field that contained a single object.

Quantification and Statistical Analysis

Construction of HD from samples

The lost HD samples were interpolated whenever the duration of sample loss was below 1.5 seconds and removed otherwise.

HD tuning curves

The head direction sample was binned into sixty bins of 6°, and a “bin estimate” of the HD tuning curve was determined as the number of spikes in each head direction bin divided by the amount of time spent in that bin. The tuning curve was then smoothed by a Gaussian kernel ($\sigma = 3$).

HD cell selection

HD cells were detected by multiple alternative methods, and a separate analysis was performed on cells classified by each of these methods indicating the same results. The methods include a generalized linear model framework for modeling spiking activity as a function of extrinsic covariates, including HD, and a shuffling procedure comparing the cell's mean resultant length or the Watson U^2 value with a chance-level outcome driven from randomly shuffled spikes (each method is described in detail later). To exclude unstable or poorly recorded clusters, only cells with a minimum overall mean firing rate of 0.1 Hz in sessions were included.

To ensure that the detected HD cell was not a byproduct of biased HD sampling from a cell with spatially selective firing, we further included the "distributive hypothesis" measure. This method measures the similarity between the observed HD tuning curve and the predicted tuning curve from the HD occupancy probability over the spatial bins. The spatial scale of the environment was segmented into 2 x 2 cm spatial bins. Within (i^{th}, j^{th}) spatial bin, the firing rate of the cell facing direction ϕ is denominated as $R_{ij}(\phi)$, and the time spent facing the direction ϕ is denominated as $T_{ij}(\phi)$. The predicted firing rate as a function of ϕ is defined as below:

$$R_{Pred}(\phi) = \sum_{i=1}^{N_x}\sum_{j=1}^{N_y} R_{ij}(\phi)\cdot T_{ij}(\phi) / \sum_{i=1}^{N_x}\sum_{j=1}^{N_y} T_{ij}(\phi) \quad (1)$$

The distributive ratio was defined as:

$$DR = \frac{1}{N}\sum_{\phi=\phi_1}^{\phi_N} \left|\ln\left(\frac{1+R_{Obs}(\phi)}{1+R_{Pred}(\phi)}\right)\right| \quad (2)$$

Where N is the number of radial bins used for the HD tuning curve (N = 60 for a bin size of 6°), N_x and N_y are the number of bins in spatial scale, and R_{Obs} is the bin estimate of the HD tuning curve. A DR value of zero indicated a complete prediction of the observed HD tuning curve by a combination of HD sampling and the spatial selectivity of cell firing. A high DR value, however, indicates that the head direction accounts for some variability of the tuning curve.

Cell classification by shuffling

A shuffling test was performed to create a statistic for evaluating whether the cell firing can be significantly explained by an external covariate HD. The spike train of individual cells was time-shifted along with the tracking samples by a variable randomly chosen between 20 s and the total trial length minus 20 s. The shifted values that were passing the length of the trial were wrapped to the beginning. Such shuffling procedure decouples the spikes from external covariates while keeping the spike timing relations intact. For the shuffled spikes, a given parameter characterizing the influence of a given covariate was calculated. This procedure was repeated 100 times, and the distribution of the outcomes was generated. The 99th percentile value of this shuffled distribution was used as the classification criterion. The parameters used for the classification of HD cells were either the mean vector length or Watson U^2.

Cell classifications by generalized linear model (GLM)

To quantify the effects and relative contribution of an extrinsic covariate (here, *i.e.*, head direction, angular head velocity, and linear speed) to the activity of a cell, while avoiding data sample binning and behavioral biases, the spiking activity was modeled as a discrete-time point process in the GLM framework under below intensity functions.

$$\lambda(t) = \lambda_0 \cdot \lambda_H(t) \cdot \lambda_A(t) \cdot \lambda_S(t)/dt \quad (3)$$

$$\lambda_0 = exp(\beta_0) \quad (4)$$

$$\lambda_H(t) = exp\left(\sum_i^{N_H} \beta_i \sin\left(i \cdot \phi(t)\right) + \beta_i' \cos\left(i \cdot \phi(t)\right)\right) \quad (5)$$

$$\lambda_s(t) = exp\left(\sum_j^{N_S} \beta_j \ S^j(t)\right) \quad (6)$$

$$\lambda_A(t) = exp\left(\sum_k^{N_A} \beta_k \ A^k(t)\right) \quad (7)$$

Where λ stands for the firing rate of the cell. $\lambda_0, \lambda_H, \lambda_A$ and λ_s stand for firing rates of baseline, head direction, angular head velocity, and linear speed components in the model, respectively. dt is the time bin size (40 ms). $\phi(t), A(t)$ and $S(t)$ are the instantaneous head direction, angular head velocity, and linear speed of the animal. N_H, N_S, N_A are the model orders respectively for head-direction, angular head velocity, and linear speed components. $\beta_0, \beta_i, \beta_i', \beta_j$ and β_k are the parameters of the model to be estimated.

The time bin size used to bin the spike trains was the same as the animal tracking sampling frequency (dt). To avoid under-sampled sections of data, AHV samples were limited to 1-99th percentile, and the very high-speed sample passing the 99th percentile threshold of the speed sample distribution was also dismissed. Speed and AHV samples were scaled over the maximum bound within (0,1) and (-1,1), respectively. HD samples were converted to radian to bound within (0, 2π). The covariate matrix was built by including all covariate elements according to the model order and the intensity functions. Model fitting was performed in MATLAB using the function "glmfit" under a Poisson distribution assumption with a log link function. The maximum order numbers were preset at $N_H = 4, N_S = 3, N_A = 3$ and all combinations of models with orders of zero up to these maximum orders were tested.

To evaluate and choose the simplest model that has the best performance in estimating a cell's spiking, we used the Bayesian Information Criterion (BIC), an information-based criterion that penalizes models with more parameters. Note that, for instance, in a one-component H model with an order of four, the number of terms is higher than in the same model with one order, and likelihood alone would not penalize this complexity.

$$BIC = k \ln(n) - 2 \ln\left(\hat{L}\right) \quad (8)$$

Where k is the number of parameters estimated by model (total number of β parameters), $\hat{L}$ is the

maximized value of the likelihood function and *n* is the number of the sample size.

Further, to avoid overfitting by including more components for each cell, we performed a ten times ten-fold cross-validation procedure by dividing the data samples into the train and test sets. Models were fit on train sets, and comparisons for model selection were made over test samples. We performed a nested method to select the best model starting from the simplest model (an intercept model) a check if any model with an extra component can perform better. Therefore, we first fitted all the models with one component (*i.e.*, four *H* models, three *S* models, and three *A* models). Among all these models, the one with the lowest average BIC value (over ten sections of test data samples) was chosen as the best model with one component and was compared to an intercept model using a one-sided signed-rank test with an α level of 0.05. If this model was significantly better than an intercept model, then the procedure would continue by comparing the best one-component model with models containing two components (*HS, HA, SA*) but only those containing the best one-component model. For instance, id the best one-component model was *H*, then the best model among all models (means a combination of all different order sizes for each component) forming either of *HS* or *HA* would be compared to the *H*-model.

Finally, a "GLM estimate" of tuning curve for a cell was reconstructed as below:

$$r_0 = \lambda_0 \cdot \overline{\lambda_H(t)} \cdot \overline{\lambda_A(t)} \cdot \overline{\lambda_S(t)}/dt \quad (9)$$

$$r_H(t) = r_0 \cdot \lambda_H(t)/\overline{\lambda_H(t)} \quad (10)$$

$$r_A(t) = r_0 \cdot \lambda_A(t)/\overline{\lambda_A(t)} \quad (11)$$

$$r_S(t) = r_0 \cdot \lambda_S(t)/\overline{\lambda_S(t)} \quad (12)$$

Where r_0 is the baseline firing rate, r_H, r_A and r_S are the reconstructed tuning curved associated with HD, AHV and speed components, respectively, and $\overline{\lambda_H(t)}, \overline{\lambda_A(t)}, \overline{\lambda_S(t)}$ are the mean values of reconstructed intensity functions. The GLM estimate of HD, AHV and speed tuning curves were constructed by calculating intensity functions (formulas 4-7) and firing rate functions (formulas 9-12) by setting values within (0, 2π), (0, 1) and (-1, 1) to the input variables $\phi(t), S(t)$ and $A(t)$, respectively.

HD tuning curve properties

Mean vector length: the magnitude of the resultant vector obtained from the head direction angles collected during the spiking of a cell.

Preferred firing direction (PFD): the angle of the resultant vector obtained from the head direction angles during the spiking of a cell.

Intra-session stability of an HD tuning curve: Sessions were divided into two 5-min sub-sessions. Stability as a correlation measure was evaluated by Pearson correlation between HD tuning curves of these sub-sessions.

Inter-session stability of an HD tuning curve: Pearson correlation value between HD tuning curved of two sessions.

Information (bits/spike): Analogous to information entropy, head-direction information was defined as:

$$I = \int_{\phi} \frac{\lambda(\phi)}{\lambda} \log_2 \left(\frac{\lambda(\phi)}{\lambda}\right) p(\phi)\, d\phi \approx \sum_i \frac{\lambda_i}{\lambda} \log_2 \left(\frac{\lambda_i}{\lambda}\right) p_i \qquad (13)$$

Where I is the information rate of the cell in bits per spike, ϕ is the head direction, $p(\phi)$ is the probability density of head pointing toward direction ϕ, $\lambda(\phi)$ is the mean firing rate when the mice head is pointing toward the direction ϕ, i is the radial bin index (i-th bin of ϕ), p_i is occupancy probability in bin i, λ_i is the mean firing rate in bin i, and λ is overall mean firing rate.

Computational Modeling

Model Overview and Purpose

To mechanistically explain how histaminergic signaling in the ADn modulates spatial memory by tuning HD cell gain, we extended a well-established neural-level model of spatial processing[58]. This framework simulates the interaction between parietal, RSC, and medial temporal areas to support spatial memory and imagery through a transformation between egocentric and allocentric reference frames.

The core extension of our model is a histamine-dependent gain control mechanism implemented within the HD cell network. This addition allows us to simulate two experimentally observed effects of histamine on ADn HD cells: a tonic modulation of baseline excitability under low cognitive demand, and a phasic enhancement of response gain during high-demand tasks such as object exploration. We simulated three histaminergic states—control, inhibition, and activation—to investigate how gain modulation in ADn propagates through the circuit, affecting the fidelity of object-position representations in downstream regions (e.g., object-vector cells in RSC) and ultimately influencing performance on an OLM task. Model predictions were subsequently validated by our experimental findings.

Model Architecture and Neural Dynamics

Our model builds upon the core architecture of the Bicanski–Burgess (BB) model, which comprises several interacting neural populations simulating key brain regions involved in spatial cognition. The network transforms an egocentric sensory representation into an allocentric memory representation and vice versa, supporting both perception and imagery.

The egocentric representation of the immediate environment is maintained in a parietal window (PW), consisting of populations coding for boundaries (PWb) and objects (PWo) in peri-personal

space (ahead, left, right of the agent). This egocentric code is transformed into an allocentric (world-centered) one via a gain-modulated transformation circuit in the RSC. This transformation is critically dependent on the current heading direction of the agent, provided by a ring attractor network of HD cells. The allocentric output of the RSC circuit drives populations of boundary vector cells (BVCs) and object vector cells (OVCs) in the medial temporal lobe, which in turn drive activity in place cells (PCs). The PCs, BVCs, and perirhinal identity cells form an attractor network that represents the spatial context and allows for pattern completion.

The dynamics of most neuronal populations are governed by continuous rate-based equations (see Parameter Values and Numerical Integration). The HD cell network is implemented as a one-dimensional ring attractor, providing a stable, persistent activity bump that tracks the agent's current heading direction. The transformation from egocentric (PWb/o) to allocentric (BVC/OVC) coordinates is performed by a multi-layered circuit in the RSC, where each sub-layer is maximally modulated by a specific head direction, effectively performing a rotation of the spatial representation.

Implementation of Histaminergic Modulation

To model the effect of histaminergic signaling from the ADn on the HD system, we implemented a gain control mechanism that modulates the output of the HD cell network. This modulation is designed to capture both the tonic (baseline) and phasic (event-triggered) components of histamine's action, as observed experimentally.

The firing rate of the HD population (r_{HD}) was calculated from its activation (ϕ_{HD}) using a standard sigmoidal function:

$$r_{HD} = 1/(1 + \exp(-2 * \beta_{HD} * (\phi_{HD} - \alpha_{HD}))) \quad (14)$$

with $\beta_{HD} = 0.1$ and $\alpha_{HD} = 5$.

Instead of modifying the internal dynamics of the HD attractor network (k_{HD}), we applied a gain factor directly to the computed r_{HD} to produce a modulated output signal ($r_{HD\_modulated}$) used by downstream areas (e.g., the RSC transformation circuit):

$$r_{HD\_modulated} = g * r_{HD} \quad (15)$$

The gain factor (g) is dynamically updated to simulate histaminergic tone:

Trigger Signal ($R_{trigger}$): A phasic neuromodulator release event was triggered when the simulated agent was within a threshold distance ($T_{trigger}$) of any object and its velocity vector was oriented towards that object.

Behavioral factor (C_{HA}): The behavioral factor of an abstract neuromodulator was modeled using a first-order kinetics equation:

$$\frac{d(C_{HA})}{dt} = \left(-C_{HA} + \alpha_{HA} * R_{trigger}\right)/\tau_{HA} \quad (16)$$

with $\tau_{HA} = 0.3\ s$ and $\alpha_{HA} = 1.0$.

Behavioral-state-dependent Gain ($\gamma_{context}$): The final g was determined by a baseline G_{global} and a component proportional to the product of the C_{HA} and the maximum activity in the object-related parietal window ($max(r_{oPW})$), scaled by a factor $\gamma_{context}$:

$$g = G_{global} * \left(1 + \gamma_{context} * C_{HA} * max(r_{oPW})\right) \qquad (17)$$

This formulation allows the gain to be dynamically enhanced during object approach, simulating a phasic response atop a tonic baseline.

This implementation allowed the gain of the HD system to be dynamically regulated in a behaviorally relevant and state-dependent manner, which we propose is a key computational function of histaminergic input to the ADn.

Simulation Protocols and Tasks

To evaluate the model's performance in spatial memory and object-location encoding, we implemented two primary simulation protocols: single-object encoding and recall, and a full OLM task. All simulations were conducted in a discretized 2D environment (22×22 units, scaled to 2×2 meters) containing one or more objects. The agent's trajectory was controlled by a velocity-based navigation algorithm with HD updating via an internal ring attractor network.

Single-Object Encoding and Recall (simflag = 10): The agent started at (5, 10) with an initial heading of π radians. The task involved navigating to a series of target locations (see targetlist in code). When the agent approached within 5.0 units of an object (parameter ObjEncThresh), encoding was triggered. During encoding, sensory inputs from the object were used to drive activity in OVCs and object-identity cells (oPRs). Hebbian learning was applied to update weights between hippocampal place cells (H), OVCs, and oPRs (H2OVCwts, OVC2Hwts, oPR2OVCwts, etc.). Recall was triggered by cueing the oPR layer with a previously encoded object identity during imagery mode (imag_flag = 1), causing the network to reactivate the corresponding OVC representation. To quantify recall accuracy, we computed the Pearson correlation between the OVC population vector during recall and during the original encoding episode. We also computed the translational accuracy of object representations by comparing egocentric (oPW) and allocentric (OVC) activity patterns after compensating for head direction shifts (see neuromodulation_effect_test.m). Data for analysis was sampled at specific time steps (e.g., step 3000 and 5000 for distal/proximal snapshots; steps 2500–6250 for activity and sparsity trends; step 10000 for imagery recall).

OLM Task *in Silicon* (simflag = 241): The agent navigated through an environment containing two objects. After initial encoding, one object was moved to a new location (at target_no = 6). The agent was then required to detect the spatial mismatch between the stored and perceived object locations. Detection was triggered when the agent re-entered the environment and approached the moved object.

Mismatch detection was quantified using a novelty signal derived from the difference in correlation between OVC population vectors for the moved object versus the unchanged object:

$$Novelty = corr\left(OVCs_{o1_{percep}}, OVCs_{o1_{imag}}\right) - corr\left(OVCs_{o2_{percep}}, OVCs_{o2_{imag}}\right) \quad (18)$$

We also computed firing sparsity of OVCs during perception and recall phases, and used a composite accuracy metric defined as:

$$Accuracy = \Delta corr * \exp\left(-10 * mean(sparsity_{OVC})\right) \quad (19)$$

where $\Delta corr = -Novelty$.

Statistical Robustness through Repeated Simulations: To ensure the statistical robustness of our model predictions, we performed 10 independent simulation trials for each of the three histaminergic conditions (control, inhibition, and activation). For each trial, we enabled intrinsic firing rate noise (noise_flag1 = 1) while keeping all other parameters identical. A unique random seed was used for each trial to generate different instantiations of the neural noise, simulating inter-trial variability analogous to biological variability in experimental preparations. Performance metrics—including the novelty signal, OVC population correlation differences, and composite accuracy—were calculated for each trial. We then computed the mean and standard deviation across the 10 trials for each condition. Statistical comparisons between conditions were performed using one-way ANOVA followed by Tukey's post-hoc test, with significance threshold set at $p < 0.05$.

Parameter Values and Numerical Integration

The vast majority of model parameters were adopted directly from the original Bicanski-Burgess publication (Bicanski & Burgess, 2018). These include all time constants, synaptic weights, and sigmoid function parameters for the core model components (PW, RSC, BVC, PC, PR populations). All simulations were run for 10 independent trials per condition to account for intrinsic variability. The firing rate noise was implemented by adding zero-mean Gaussian noise with amplitude proportional to the baseline firing rate of each neural population (20% of baseline activity).

Table 1: Parameters introduced or modified for simulating histaminergic modulation.

Parameter	Description	Value	State
τ_{neuro}	Time constant for neuromodulator dynamics	0.3 s	All
α_{neuro}	Scaling factor for trigger signal	1.0	All
$T_{trigger}$	Distance threshold for triggering phasic release	7 units	All

Parameter	Description	Value	State
G_{global}	Baseline tonic gain	0.91	Control
		0.83	Inhibition
		1.00	Activation
$\gamma_{context}$	Amplitude of phasic gain modulation	0.5	Control
		0.0	Inhibition
		1.0	Activation

Whole-brain mapping and quantitative analysis of retrogradely labeled neurons

Whole-brain registration and atlas alignment.

Every fifth section throughout the entire brain was imaged using VS120 (Olympus Corpration, Japan) to capture the tdTomato signal. The resulting image series for each brain were processed using the ABBA (Aligning Big Brains and Atlases) plugin in FIJI[59]. In brief, the native space images were manually aligned to the Allen Mouse Brain Common Coordinate Framework (CCFv3) reference atlas. A rigid transformation was first applied for initial coarse alignment, followed by an affine transformation for fine-scale adjustment, ensuring optimal registration of the individual brain sections to the corresponding atlas plates.

Automated cell detection and quantification in QuPath.

The atlas-aligned images, along with the propagated anatomical annotations from the ABBA registration, were imported into QuPath (version 0.6.0) to create a whole-brain project for each animal. To identify and count retrogradely labeled neurons, an automated detection pipeline was established. A 'Positive Cell Detection' algorithm was applied, which was optimized based on a subset of manually annotated cells to maximize accuracy. The detection parameters were set as follows: the detection image was set to the red channel; the background radius was set to 8.0 μm; the median filter radius was 5 μm; the sigma for Gaussian smoothing was 1.5 μm; and the intensity threshold was set to 100 to distinguish positive signals from background. The minimum and maximum cell area were constrained to 50 μm² and 400 μm², respectively, to exclude non-cellular objects and debris. The same parameter set was applied consistently across all sections and all three animals. The anatomical identity of each detected cell was automatically assigned based on the imported atlas annotations

from ABBA.

Data aggregation and analysis.

For each animal, the counts of labeled neurons from all analyzed sections were aggregated by brain region according to the Allen Brain Atlas hierarchy. The raw cell counts for each region were then normalized to account for sampling frequency, resulting in the total estimated number of labeled neurons per brain region per animal. The final data presented represent the mean ± standard error of the mean (SEM) across the three biological replicates (N = 3 mice).

Supplementary Figures

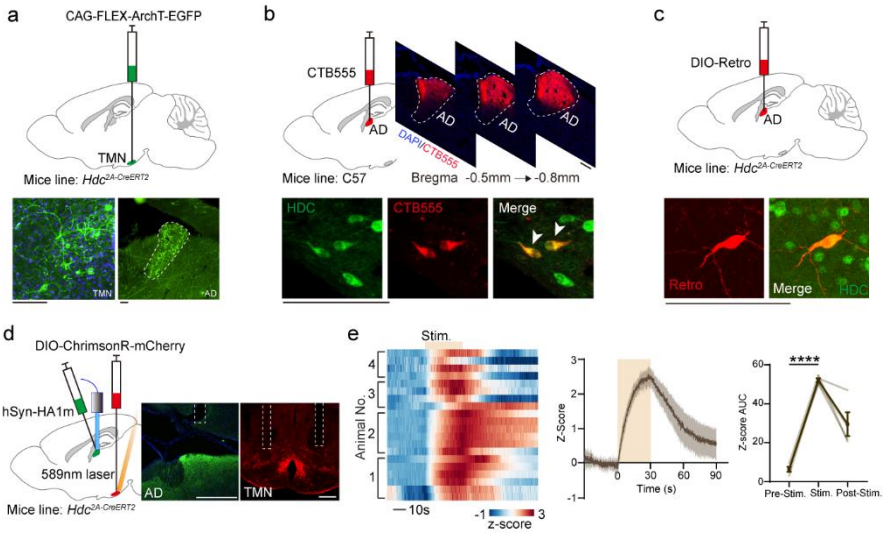

Supplementary Figure S1 | Functional connectivity between TMN and ADn.

a, Viral strategy and validation for anterograde labeling of histaminergic terminals. *Top:* Schematic of AAV injection into the TMN of *HDC-Cre^{ERT2}* mice. *Bottom Left:* Representative image showing expression of AAV-FLEX-ArchT-EGFP in the TMN. *Bottom Right:* Representative images showing EGFP+ histaminergic fibers and terminals in the anterodorsal (ADn) and anteroventral (AV) thalamic nuclei. Scale bar, 100 μm.

b, Retrograde tracing of ADn inputs using CTB. *Top:* Schematic of CTB-555 injection into the ADn of a wild-type mouse and a representative image of the injection site. *Bottom:* Representative image showing retrogradely labeled histaminergic neurons (CTB-555+, white arrows) in the TMN. Scale bar, 100 μm.

c, Retrograde viral tracing of TMN neurons projecting to the ADn. *Top:* Schematic of Retro-FLEX-mCherry injection into the ADn of *HDC-Cre^{ERT2}* mice. *Bottom:* Representative image showing retrogradely labeled, mCherry-expressing histaminergic neurons in the TMN. Scale bar, 100 μm.

d-e, Optogenetic activation of TMN histaminergic neurons evokes histamine release in the ADn.

d, *Top:* Schematic of dual-virus injection and dual-fiber implantation: AAV-FLEX-ChrimsonR-mCherry in the TMN and AAV-hSyn-HA1m in the ADn. *Bottom:* Histological verification of ChrimsonR expression in the TMN and fiber placement in the ADn and TMN. Scale bar, 500 μm.

e, Histamine sensor response to optical stimulation (γ = 589 nm, 30 s on, 10 Hz, 10 ms) of TMN histaminergic neurons. *Left:* Heatmap of Z-scored ΔF/F sensor signals across trials (20 trials from N = 4 mice). *Middle:* Average Z-scored ΔF/F trajectory (mean ± s.e.m.); shaded area indicates the light stimulation period. *Right:* Area under the curve (AUC) analysis of the sensor response for pre, during and post the stimulation period. One-way ANOVA, Tukey's multiple comparison test.

All error bars and shaded areas represent mean ± s.e.m. * $P \leq 0.05$; ** $P \leq 0.01$; *** $P \leq 0.001$; **** $P \leq 0.0001$; n.s., not significant.

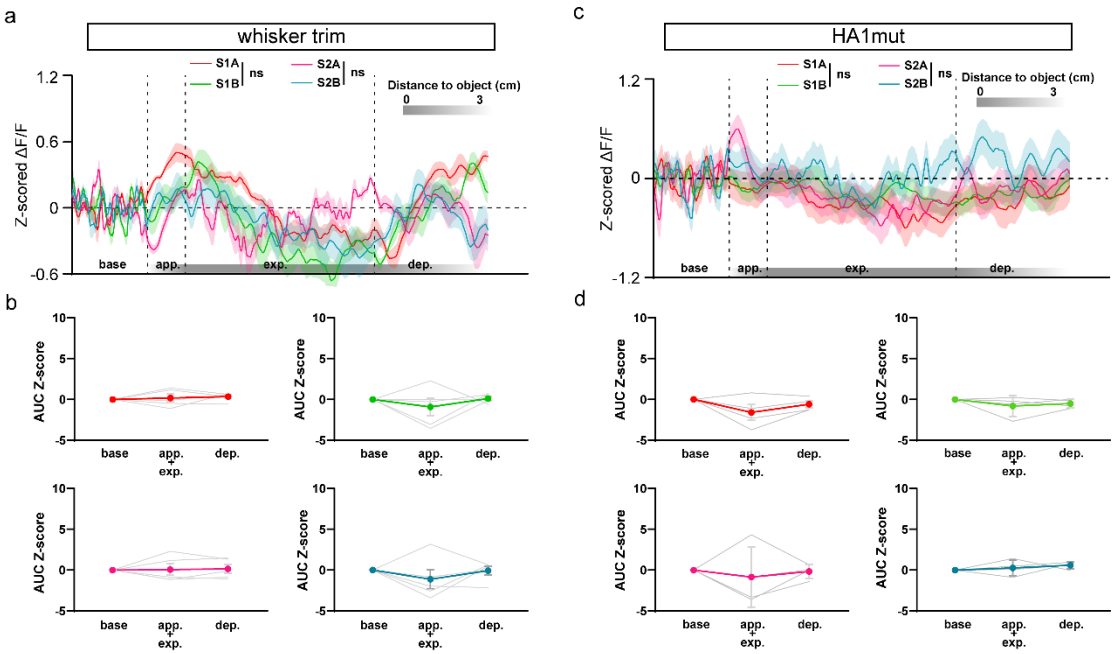

Supplementary Figure S2 | Somatosensory input via whiskers is necessary for object-triggered histamine release in the ADn.

a, Population data of Z-scored ΔF/F trajectories of the histamine sensor aligned to the onset of object approach (time = 0) in whisker-trimmed mice. Traces are shown for both objects during the first and second exposure stages. No significant modulation was observed during object exploration following whisker removal. Two-way RM ANOVA.

b, AUC analysis for the exploration epochs defined in **a**. No significant differences were found across objects or stages. RM one-way ANOVA, Tukey's multiple comparisons test, n = 5 mice.

c, Control recordings using a mutated, histamine-insensitive sensor (HA1mut) in the ADn during the object location memory (OLM) task. Population data of Z-scored ΔF/F trajectories show no significant fluctuations during object exploration epochs.

d, AUC analysis for the exploration epochs defined in **c**. No significant differences were found. RM one-way ANOVA, Tukey's multiple comparisons test, n = 4 mice.

All error bars and shaded areas represent mean ± s.e.m. n.s., not significant.

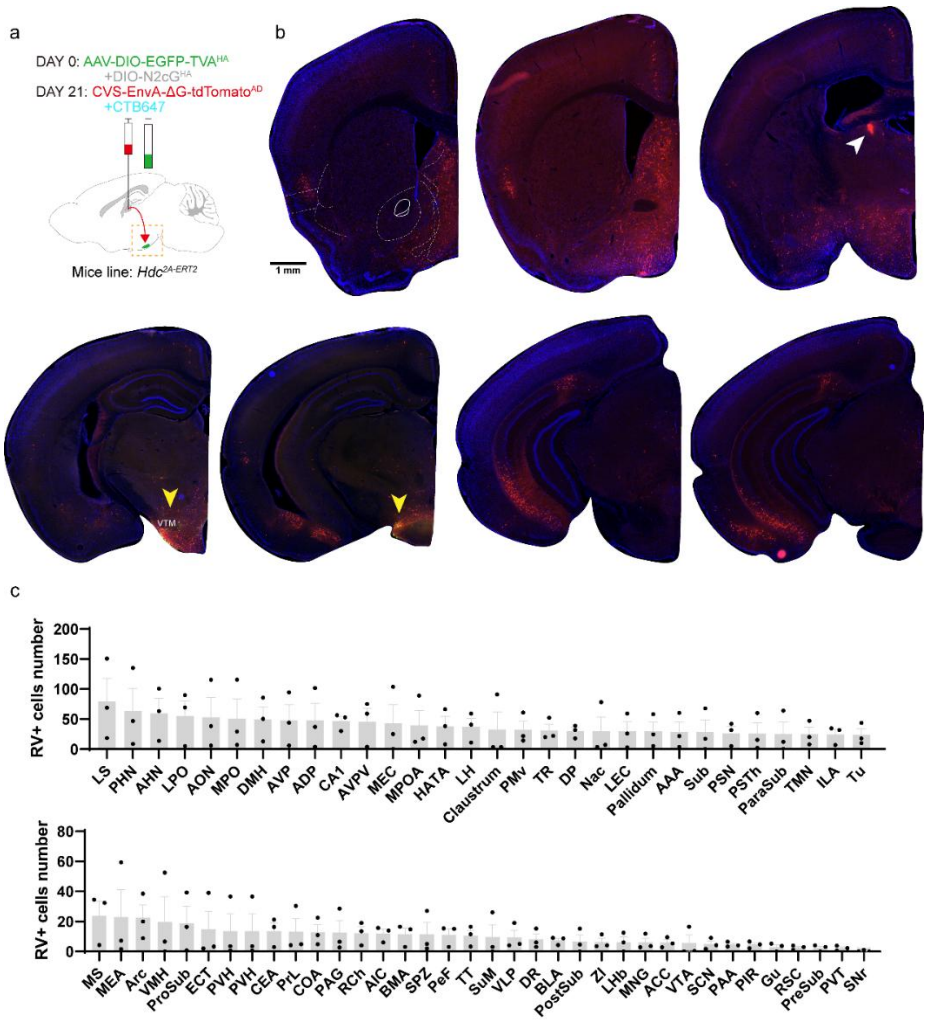

Supplementary Figure S3 | Whole-brain quantitative mapping of monosynaptic inputs to ADn-projecting histaminergic neurons.

a, Viral strategy for trans-neuronal, triple retrograde tracing from ADn-projecting histaminergic neurons in the TMN of *HDC-Cre*^{ERT2} mice.

b, Whole-brain map showing representative regions containing neurons providing monosynaptic input to ADn-projecting histaminergic neurons (labeled with tdTomato). Insets: Representative image of the viral injection site in the ADn (white arrow) and the starter cells (co-expressing GFP and tdTomato, yellow arrows) in the TMN. Scale bar, 1 mm (applicable to whole-brain images and insets).

c, Quantitative summary of monosynaptic inputs to ADn-projecting histaminergic neurons. Bar plot ranks all 64 identified brain regions by the mean number of tdTomato+ input neurons per mouse (N = 3 mice), from the highest to the lowest. Data are presented as mean ± s.e.m.

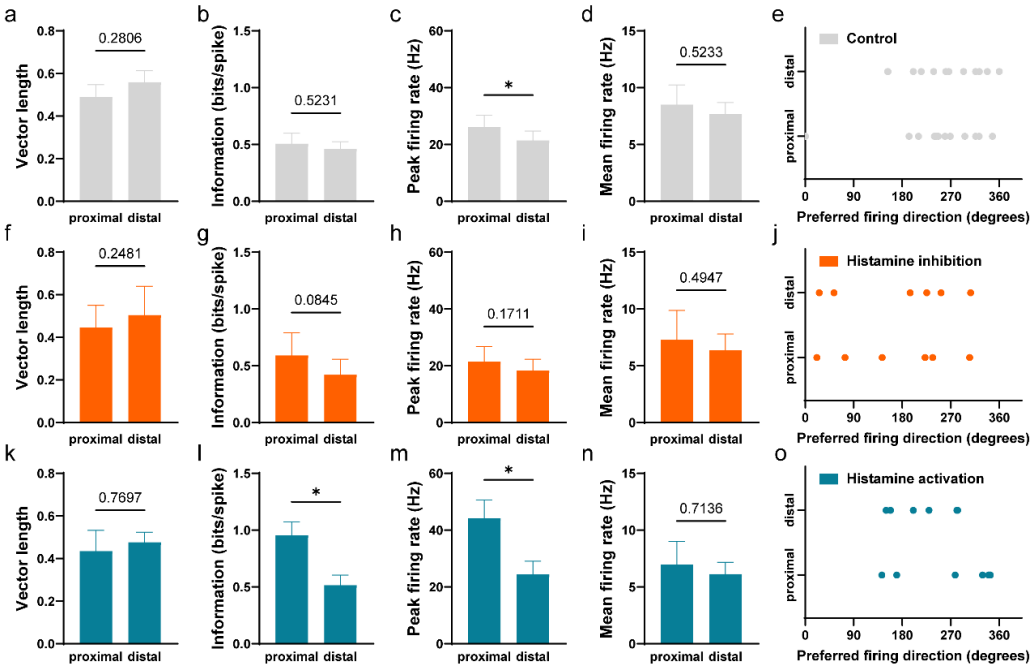

Supplementary Figure S4 | Histaminergic signaling bidirectionally modulates the object-associated tuning of anterodorsal thalamic head-direction cells.

a-e, Spatial tuning properties under control (saline) conditions. (N = 12 cells)

a, Population vector length for proximal and distal epochs. Unpaired t-test. **b,** Spatial information content. Unpaired t-test. **c,** Peak firing rate was significantly higher in proximal epochs compared to distal. Unpaired t-test. **d,** Mean firing rate. Unpaired t-test. **e,** Preferred firing direction. Unpaired t-test.

f-j, Enhanced spatial tuning following activation of histaminergic neurons. (N = 6 cells)

f, Population vector length. Unpaired t-test. **g,** Spatial information content. Unpaired t-test. **h,** Peak firing rate. Unpaired t-test. **i,** Mean firing rate. Unpaired t-test. **j,** Preferred firing direction. Unpaired t-test.

k-o, Attenuated spatial tuning following inhibition of histaminergic neurons. (N = 6 cells)

k, Population vector length. Unpaired t-test. **l,** Spatial information content was significantly lower in proximal epochs following inhibition. Unpaired t-test. **m,** Peak firing rate was significantly higher in proximal epochs. Unpaired t-test. **n,** Mean firing rate. Unpaired t-test. **o,** Preferred firing direction. Unpaired t-test.

All data are presented as mean ± s.e.m. Significant differences between proximal and distal epochs are indicated: * $P \leq 0.05$; ** $P \leq 0.01$; *** $P \leq 0.001$; n.s., not significant.

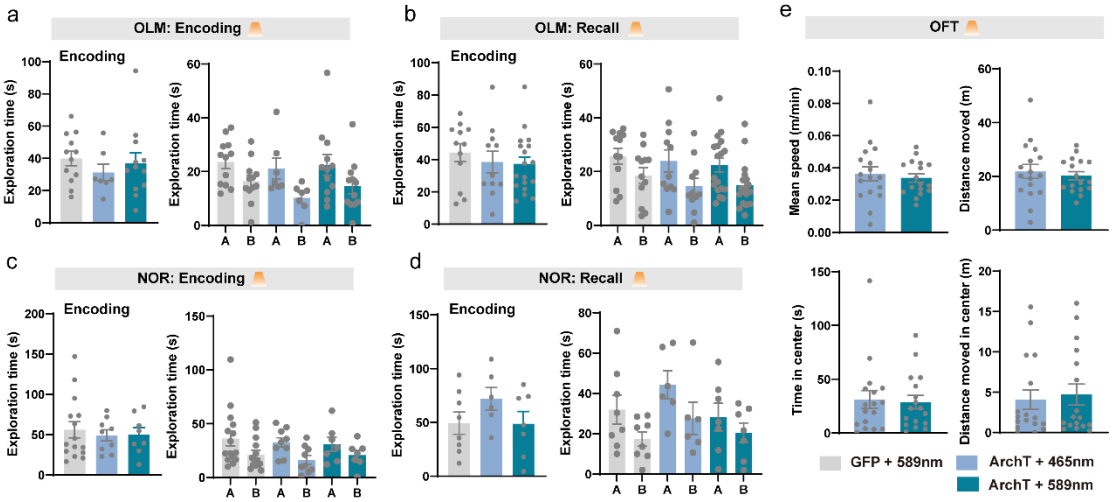

Supplementary Figure S5 | Optogenetic inhibition of histaminergic terminals in the ADn does not alter basal exploratory locomotion, or anxiety-like behavior.

a, Performance on the object location memory (OLM) encoding phase with optogenetic inhibition. *Left:* Total exploration time for all objects. *Right:* Exploration time for each individual object (A, B). No significant differences were found between groups. One-way ANOVA, Tukey's multiple comparison test, n as in Fig. 6d.

b, Performance on the OLM encoding phase with optogenetic inhibition during recall phase. *Left:* Total exploration time. *Right:* Exploration time for each individual object (A, B). No significant differences were found between groups. One-way ANOVA, Tukey's multiple comparison test, n as in Fig. 6e.

c, Performance on the novel object recognition (NOR) encoding phase with optogenetic inhibition. *Left:* Total exploration time for all objects. *Right:* Exploration time for each individual object (A, B). No significant differences were found between groups. One-way ANOVA, Tukey's multiple comparison test, n as in Fig. 6g.

d, Performance on the NOR encoding phase with optogenetic inhibition during recall phase. *Left:* Total exploration time. *Right:* Exploration time for each individual object (A, B). No significant differences were found between groups. One-way ANOVA, Tukey's multiple comparison test, n as in Fig. 6h.

e, Performance in the open field test (OFT) following optogenetic inhibition. Metrics include: mean speed (first 10 min), total distance moved (first 10 min), time spent in the center (first 5 min), and distance moved in the center (first 5 min). No significant differences were found between control and inhibition groups, indicating that inhibition did not affect locomotor activity or anxiety-like behavior. Unpaired t-test, n = 17, 17 mice.

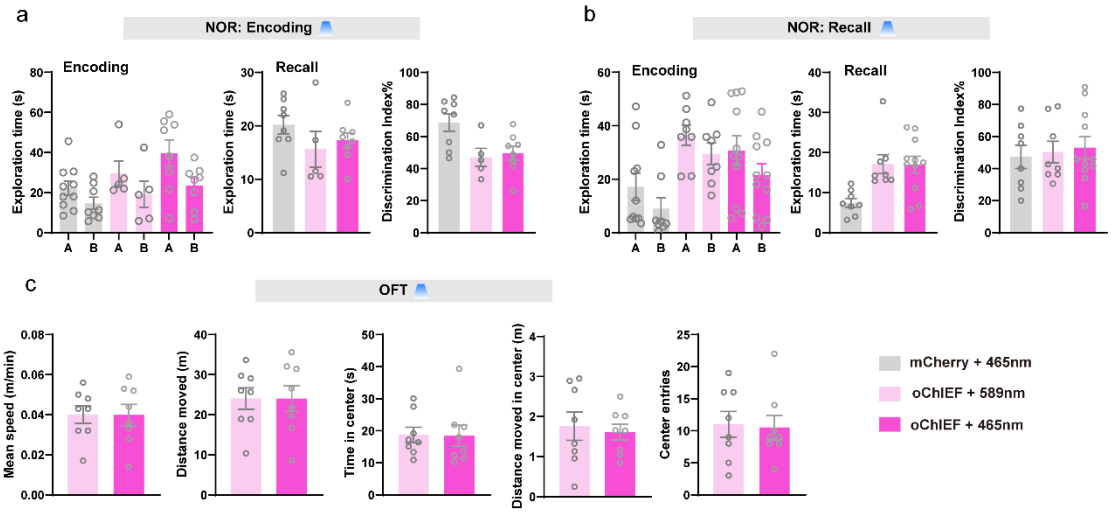

Supplementary Figure S6 | Optogenetic activation of histaminergic terminals in the ADn does not alter basal exploratory locomotion, or anxiety-like behavior.

a, Performance on the NOR task with optogenetic activation during the encoding phase. *Left:* Exploration time for each object during the encoding phase. *Middle:* Total exploration time during the recall phase. *Right:* Discrimination index during the recall phase. No significant differences were found between groups One-way ANOVA, Tukey's multiple comparison test, n = 8, 5, 8 mice.

b, Performance on the NOR task with optogenetic activation during the recall phase. *Left:* Exploration time for each object during the encoding phase. *Middle:* Total exploration time during the recall phase. *Right:* Discrimination index during the recall phase. No significant differences were found between groups. One-way ANOVA, Tukey's multiple comparison test, n = 10, 8, 11 mice.

c, Performance in the OFT following optogenetic activation. Metrics include: mean speed (first 10 min), total distance moved (first 10 min), time spent in the center (first 5 min), distance moved in the center (first 5 min), and number of entries to the center (first 5 min). No significant differences were found between control and activation groups, indicating that activation did not affect locomotor activity or anxiety-like behavior. Unpaired t-test, n = 8, 8 mice.

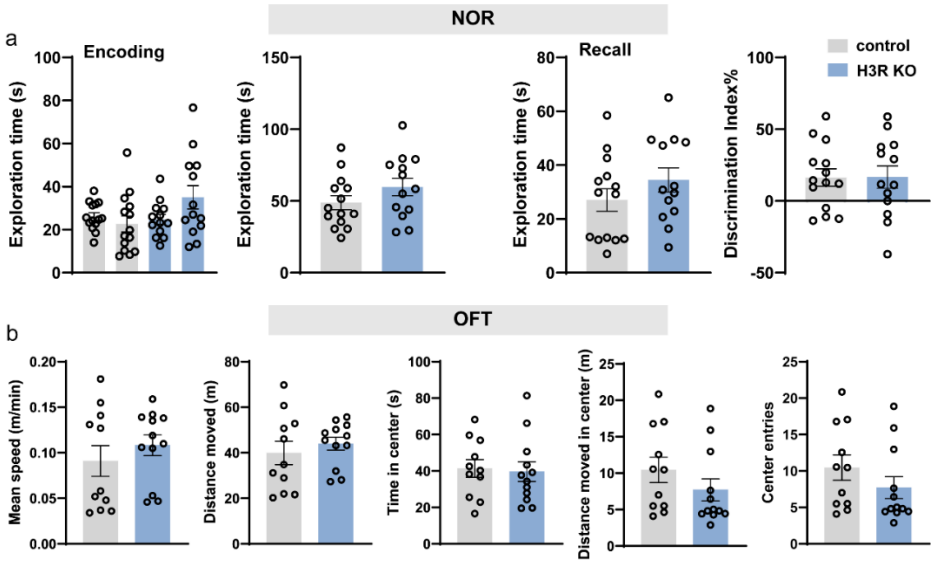

Supplementary Figure S7 | Conditional knockout of H3R in the ADn does not alter baseline locomotor, anxiety-like, or novel object recognition behaviors.

a, Performance on the NOR task following H3R knockout. *Left:* Exploration time for each object and total during the encoding phase. *Right:* Total exploration time and discrimination index during the recall phase. No significant differences were found between groups, indicating that loss of H3R did not affect novel object recognition. Unpaired t-test, n = 14, 13 mice.

b, Performance in the OFT following H3R knockout. Metrics include: mean speed (first 10 min), total distance moved (first 10 min), time spent in the center (first 5 min), distance moved in the center (first 5 min), and number of entries to the center (first 5 min). No significant differences were found between control and knockout groups, indicating that loss of H3R did not affect locomotor activity or anxiety-like behavior. Unpaired t-test, n = 11, 12 mice.

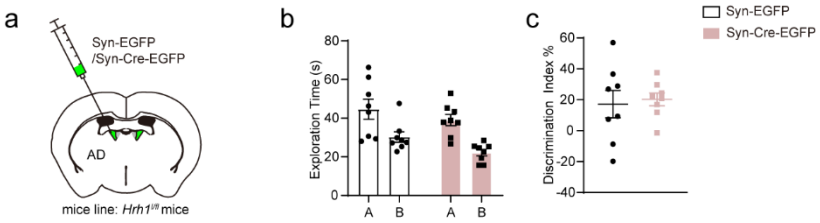

Supplementary Figure S8 | Depletion of H1Rs in the ADn does not impair object location memory.

a, Schematic of AAV injection into the ADn of *Hrh1*$^{fl/fl}$ mice for conditional knockout of the H1 receptors.

b, Exploration time for each object during the encoding phase of the OLM task. No significant difference was found between groups. Unpaired t-test, $n_{GFP/Cre}$ = 8/8 mice.

c, Discrimination index during the recall phase of the OLM task. Knockout of the H1 receptor in the ADn did not significantly impair spatial memory performance compared to the control group. Unpaired t-test, $n_{GFP/Cre}$ = 8, 8 mice.

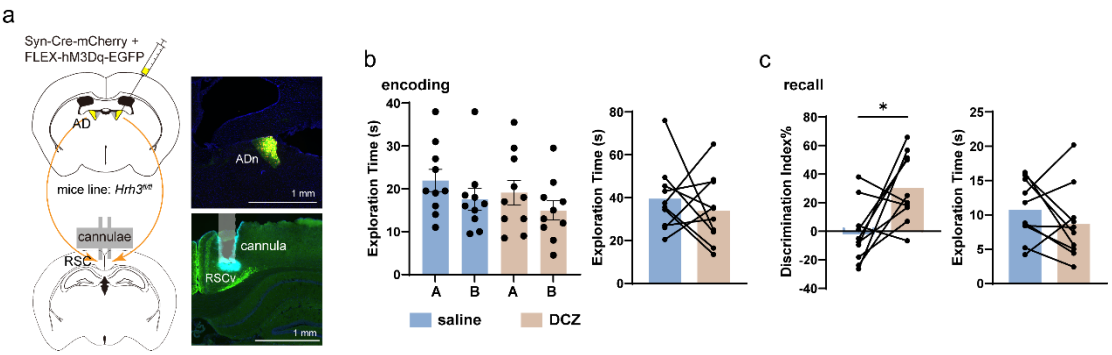

Supplementary Figure S9 | Chemogenetic activation of ADn-RSC projections rescues spatial memory deficits in H3R conditional knockout mice.

a-c, Functional validation of a downstream target: Activating the projections from H3R-knockout ADn neurons to the retrosplenial cortex (RSC) rescues spatial memory deficits.

a, *Left:* Schematic of bilateral viral injection in the ADn of *Hrh3*$^{fl/fl}$ mice. Viruses express Cre recombinase (for H3R knockout) and the chemogenetic actuator hM3Dq. *Right:* Schematic of bilateral cannula implantation in the RSC for infusion of the hM3Dq agonist DCZ or saline.

b, Exploration during the encoding phase of the OLM task following intra-RSC infusion. No significant differences were found between saline and DCZ groups. Unpaired t-test, $n_{saline/DCZ}$ = 10, 10 mice.

c, Performance during the recall phase. *Left:* Activation of ADn-RSC projections significantly rescued the discrimination index. *Right:* Total exploration time was unchanged. Unpaired t-test, $n_{saline/DCZ}$ = 10, 10 mice.

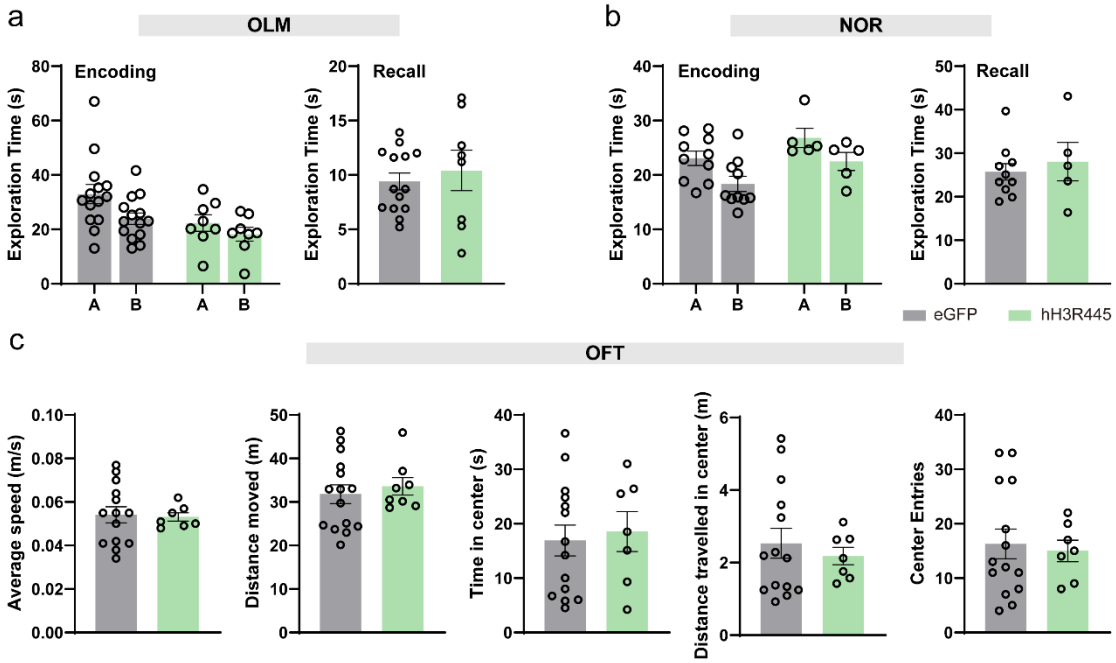

Supplementary Figure S10 | Overexpression of H3R445 in the ADn does not alter baseline exploration, locomotor activity, or anxiety-like behavior.

a, Exploration behavior during the OLM task following H3R445 overexpression. *Left:* Exploration time for each object during the encoding phase. *Right:* Total exploration time during the recall phase. No significant differences were found between groups. Unpaired t-test, n = 14, 8 mice.

b, Exploration behavior during the NOR task following H3R445 overexpression. *Left:* Exploration time for each object during the encoding phase. *Right:* Total exploration time during the recall phase. No significant differences were found between groups. Unpaired t-test, n = 10, 10 mice.

c, Performance in the OFT following H3R445 overexpression. Metrics include: mean speed (first 10 min), total distance moved (first 10 min), time spent in the center (first 5 min), distance moved in the center (first 5 min), and number of entries to the center (first 5 min). No significant differences were found between groups, indicating that H3R445 overexpression did not affect locomotor activity or anxiety-like behavior. Unpaired t-test, n = 14, 7 mice.

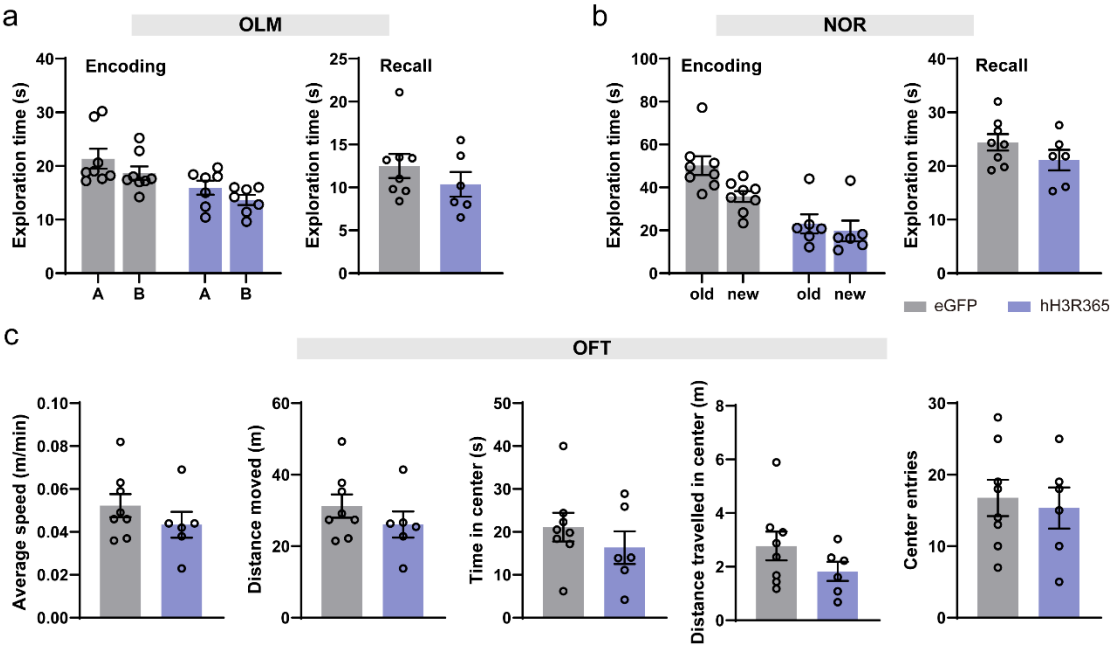

Supplementary Figure S11 | Overexpression of H3R365 in the ADn does not alter baseline exploration, locomotor activity, or anxiety-like behavior.

a, Exploration behavior during the OLM task following H3R365 overexpression. *Left:* Exploration time for each object during the encoding phase. *Right:* Total exploration time during the recall phase. No significant differences were found between groups. Unpaired t-test, n = 8, 6 mice.

b, Exploration behavior during the NOR task following H3R365 overexpression. *Left:* Exploration time for each object during the encoding phase. *Right:* Total exploration time during the recall phase. No significant differences were found between groups. Unpaired t-test, n = 8, 6 mice.

c, Performance in the OFT following H3R365 overexpression. Metrics include: mean speed (first 10 min), total distance moved (first 10 min), time spent in the center (first 5 min), distance moved in the center (first 5 min), and number of entries to the center (first 5 min). No significant differences were found between groups, indicating that H3R365 overexpression did not affect locomotor activity or anxiety-like behavior. Unpaired t-test, n = 8, 6 mice.